International Journal of Engineering Trends and Technology
ISSN: 2231 – 5381 / https://doi.org/10.14445/22315381/IJETT-V71I2P204

Volume 71 Issue 2, 27-38, February 2023

Original Article

Gorilla Troops Optimizer with Deep Learning-Based Thyroid Cancer Classification on Histopathological Images

M. Gokilavani[1], M. Sriram[2], S.P. Vijayaraghavan[3], T. Jaya[4]

[1,2]*Department of CSE, BIHER, Chennai, India.*
[3]*Department of ECE, BIHER, Chennai, India.*
[4]*Department of CSE, VEL'S university, Chennai, India.*

[1]*Corresponding Author : mailme.gokilavani@gmail.com*

Received: 12 November 2022 Revised: 10 January 2023 Accepted: 25 January 2023 Published: 25 February 2023

Abstract *- The thyroid gland serves a vital role in regulating various body functions, namely energy expenditure, metabolism, and organ function, such as the heart and brain. Thyroid cancer refers to a cancer of the thyroid gland and is a commonest endocrine cancer. A pathologist can detect thyroid carcinoma on the basis of the visual inspection of tissue samples prepared on microscopic slides. Machine learning (ML) is increasingly employed in the medical imaging fields and for pathological diagnosis of various diseases. A deep convolutional neural network (DCNN) is a kind of ML, such as a specific artificial neural network resembling the multi-layered human cognitive system. Various studies have examined the application of DCNN to assess pathological images. This paper introduces a novel Gorilla Troops Optimizer with Deep Learning Based Thyroid Cancer Classification on Histopathological Images (GTODL-TCHI) model. The presented GTODL-TCHI model majorly analyses the HIs for the identification and classification of thyroid disease. Initially, the GTODL-TCHI model applies the image denoising procedure using the non-local mean filtering (NLMF) technique. In addition, the pre-processed images are then segmented using a fully convolutional network (FCN). Besides, the GTO algorithm with a densely connected network (DenseNet121) method can be implied to produce feature vectors. Finally, the classification of features takes place using a stacked sparse autoencoder (SSAE) model. The performance validation of the GTODL-TCHI method can be tested using the HI dataset. The results stated the significant performance over the recent state of art DL models.*

Keywords *- Thyroid disease, Histopathological images, Computer aided diagnosis, Deep learning, Image processing.*

1. Introduction

Recently, thyroid cancer has been increasing rapidly among all solid malignant cancers. The comparatively high incidence, which continues to grow, becomes thyroid cancer, the most common endocrine malignancy globally, recently listed as the fifteenth most prevalent tumor among men and seventh most prevalent tumor among females [1]. Thyroid cancer research turns out to be a matter of widespread concern in society and the medical community [2]. The prognosis of thyroid cancer becomes a difficult task. Many thyroid cancers were revealed as thyroid nodules that were often identified accidentally at the time of the neck diagnostic imaging [3]. Several thyroid nodules were heterogeneous, with several internal elements that may confuse radiotherapists and doctors with its numerous echo paradigms in thyroid nodules ultrasonography [4,22]. To improvise the prognosis rate and minimize the loss that occurred by the improper diagnosis, computer-aided diagnosis (CAD) was projected, which is helpful for the medical practitioner in discriminating nodules from malignancy or benign.

The pathological prognosis of respected specimens becomes a golden standard for cancer diagnosis [24]. In recent times, the massive major pathological tissue sections were obtained by diagnosticians, and specimen collections were compiled over a longer duration, which can be utilized for medical prognosis [6,9]. Yet, physical differential diagnosis of thyroid cancer Histopathological images will remain a challenging factor for 3 key reasons; one is the capability to properly prognoses samples importantly based on the professional background and pathologist experience, and these experiences may not be obtained quickly, and the second reason was the work is time taking, tedious, costly, and the last reason is it becomes a challenge for a human eye for distinguishing subtle variations in tissues [7]; therefore, pathologists could experience exhaustion, that results in misdiagnosis. Therefore, the accurate histopathology prognosis of thyroid nodules will remain difficult.

Over the past few decades, machine learning (ML)-related solutions have been devised and grabbed much more attention from medical imaging researchers [5,8]. Medical

images comprise key information which imitates the underlying physiology of cancers that might be unnoticeable to the human eyes. Currently, convolutional neural network (CNN) systems have succeeded in examining medical imaging classification errands, including diabetic retinopathy classification and skin lesion evaluations and in the observation of severe neurologic events [22]. DL methods' potential numbers and types have exploded in the past few years. Conventional feature extraction techniques need clear knowledge and a complete design for defining hand-crafted features. On the other hand, CNN methods optimize and derive features automatically from data sets based on defined objectives [10].

This paper introduces an innovative Gorilla Troops Optimizer with Deep Learning Based Thyroid Cancer Classification on Histopathological Images (GTODL-TCHI) model. The presented GTODL-TCHI model majorly analyses the HIs for the identification and classification of thyroid disease. Initially, the GTODL-TCHI model applies the image denoising procedure using the non-local mean filtering (NLMF) technique. In addition, the pre-processed images are then segmented using a fully convolutional network (FCN). Besides, the GTO algorithm with a densely connected network (DenseNet121) model is applied to produce feature vectors. Finally, the classification of features takes place using a stacked sparse autoencoder (SSAE) model. The performance validation of the GTODL-TCHI technique can be tested with the help of a HI dataset.

2. Literature Review

Han et al. [11] suggest an active classifying technique for papillary thyroid carcinoma (PTC) categorization of pathological images for dividing thyroid pathological imageries as normal thyroid pathological imageries and PTC. The researchers use the attention system for compiling pathological images and distinct magnification aspects that reflect the prognosis process of thyroid tumor under the microscope. Meanwhile, the authors use the representative and uncertain information offered by CNN for determining the most useful samples for annotation, which could minimize labelling costs. In [12], the authors project a workflow to display that BRAFV600E mutation grade is straight forecasted from Histopathological images with DL. This technique majorly contains 2 steps, mutation classification and tumor detection; both have a CNN. The information extracted from the two steps was compiled for predicting mutation.

Wang et al. [13] present the theory of CNN regarding the difficulty in detecting the ultrasound image of PTC and recommends a technique that could automatically identify the ultrasound image of PTC. In the context of the requirement of ultrasonic image identification of PTC, a Fast Region-related CNN technique (Faster RCNN) can be improvised and normalized by linking the fifth- and fourth layers of the shared convolutional layers in a Fast RCNN network. After which, a multistage ultrasound image can be utilized during input. Liu et al. [14] suggest a feature-extracting technique for ultrasound images related to CNNs and try to present more useful semantic features to the categorization.

Chi et al. [15] introduce a CAD system to classify thyroid nodules in ultrasound images. The researchers use the DL technique for extracting features from thyroid ultrasound images. Ultrasound imageries have been pre-processed to calibrate their scale and eliminate the artifacts. A pretrained Google Net method can be finely tuned after the pre-processed image samples, resulting in better feature extraction. Song et al. [26] focus on identifying PMC and PTC with the help of Raman spectroscopy. The authors may collect serum Raman spectra from 31 patients having PMC and 16 patients having PTC. At first, the gathered imbalanced data are pre-processed using the synthetic minority over-sampling technique (SMOTE). After which, data that is equalized are dimensionality minimized by principal component analysis (PCA). At last, the data which is processed has been entered in the random forest (RF) and one decision tree (DT) classification, constructed on the idea of the Adaptive Boosting (Adaboost) and Boosting ensemble technique devised on the ideology of bagging ensemble for classification.

3. The Proposed Model

This study devised a novel GTODL-TCHI model to recognize the presence of the thyroid on HIs. The presented GTODL-TCHI model primarily utilized the NLMF technique to eradicate the existence of noise, and then the FCN model was utilized to segment the images. Then, the DenseNet-121 model is utilized to derive feature vectors, and its hyperparameters are tuned using the GTO algorithm. At last, the SSAE method can be implied to categorize the class labels of the input HIs. Fig. 1 depicts the overall process of the GTODL-TCHI algorithm.

3.1. Denoising Process

The presented GTODL-TCHI model primarily utilized the NLMF technique to eradicate the noise. It upgrades the weight value of normal pixels. The weight of all the pixels is based merely on the distance between intensity grey level vectors and target pixels. In all the pixels, denoised images are calculated as follows:

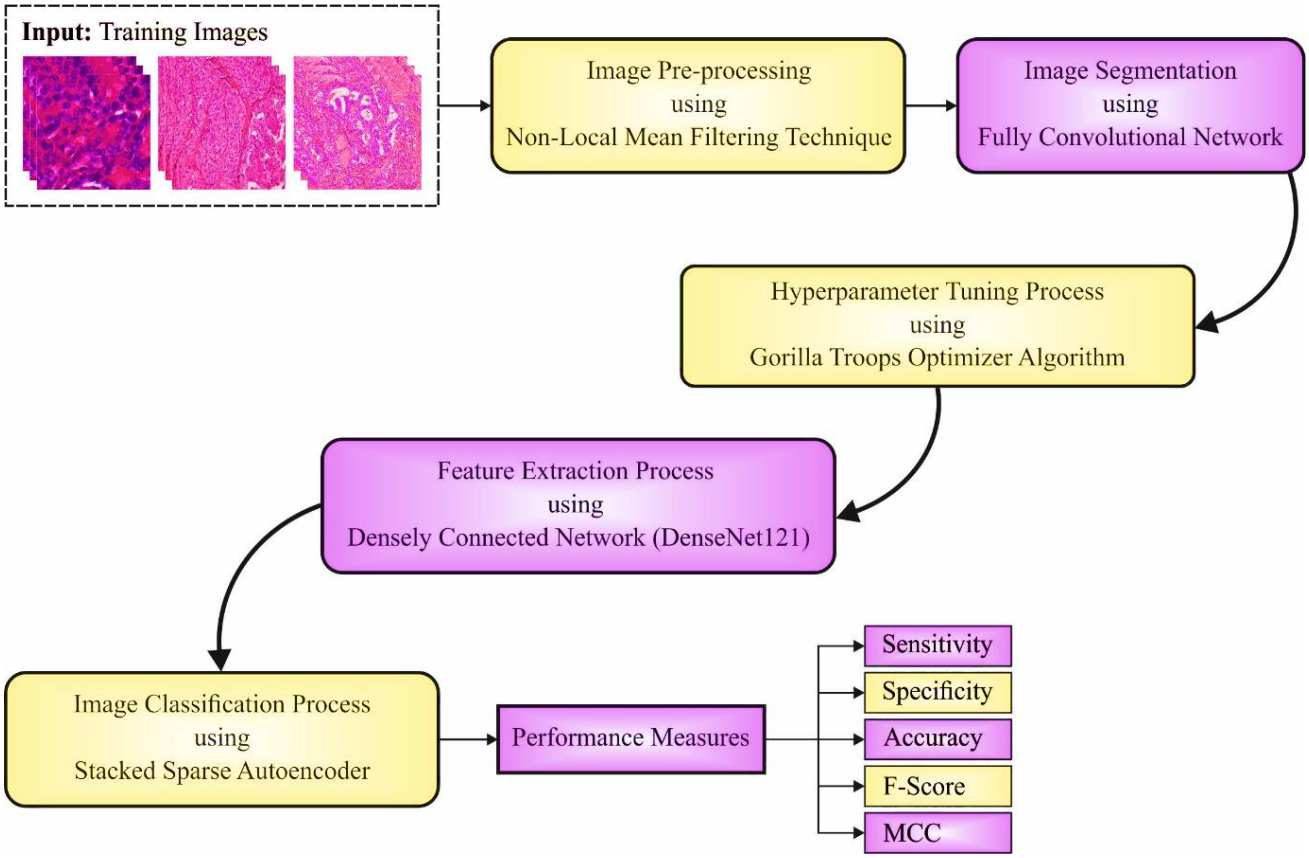

Fig. 1 Overall process of the GTODL-TCHI approach

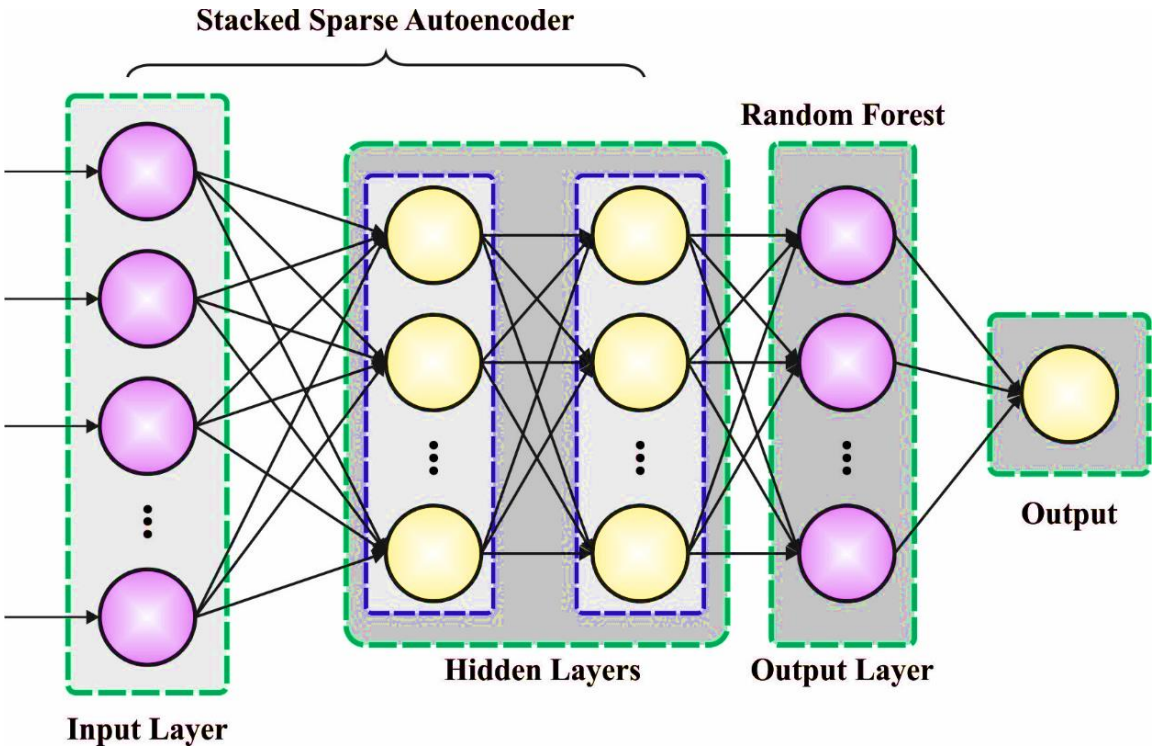

Fig. 2 Framework of SSAE

$$M(i,j) = \sum_{j \in D} D(i,j) w(i,j) \quad (1)$$

Let j be the noise images, and M denotes the denoised images. With the following circumstance, $0 \leq w(i,j) \leq 1$ weight is achieved. Weighted averages of whole pixels depend on the judgment among the locality of **i** and **j** pixels.

3.2. Image Segmentation using FCN Model

Once the images are pre-processed, the next stage is to perform image segmentation using the FCN model. The network comprises deconvolutional (expansion) and convolution (contraction) blocks [17]. Every convolutional or deconvolutional block comprises residual, primary, and secondary convolution layers. The convolutional process takes place in every convolution layer. There exists a max pooling layer after every convolutional block that halves the output size.

In contrast, there is a bi-linear up-sampling layer after every deconvolutional block that doubles the output's size after every block. In the convolutional operation, we set each stride equivalent to one. The convolutional mode has been set to 'same', which results in padding the input so that the output has a similar size as the actual input. 393 filters implement each convolutional and deconvolutional process, i.e., upgraded by backpropagation at the end of every mini-batch in the trained phase. The rectified linear unit (ReLU) is employed as the activation function for each convolutional layer. This activation function offers advantages compared to other linear or nonlinear activation functions. In contrast to a linear one, ReLU offers high expressiveness in the deep network, and contrasted with a nonlinear one, ReLU does not undergo the gradient vanishing problems and sustains stable convergence speed. The sigmoid function implements pixel-wise semantic segmentation in the final stage.

3.3. Feature Extraction

Then, the DenseNet-121 model is utilized to derive feature vectors, and the GTO algorithm tunes its hyperparameters. The DenseNet-121 infrastructure was employed during this case as the foundation [18]. In addition, the transfer learning (TL) approach was utilized in the Dense Net framework to improve the system efficiency. Dense Net needs some parameters compared with standard CNN approaches as it could not be needed for a redundant feature map. The fundamental model of Dense Net structure refers to a feature reprocessed to extremely compact versions. Accordingly, it needs variables related to another CNN method since no feature map was repeated. If CNN drives more, it can face challenges. Dense Net generates this connectivity much more simpler by basically interconnected every layer straightforwardly with all the layers. In Dense, Nets employ the network ability with reemploying features. Each layer from Dense Net attains more input on all the prior layers and transfers their feature maps to the following layers.

To optimally modify the hyperparameter values of the DenseNet-121 model, the GTO algorithm is utilized. The GTO algorithm simulates 5 strategic alternatives to explain the exploration and exploitation processes, which are briefly discussed [27].

3.3.1. Exploration Phase

In GTO, each gorilla individual is represented as a solution candidate. However, each operational stage selects the global optimum solution as a silverback. For the developmental phase, three different techniques are utilized. The initial one is the movement to an unidentified destination to increase GTO exploration, whereas the second technique is the movement of other gorillas to improve the reliability of exploitation and exploration. Furthermore, the third technique is the gorilla's movement in the path of a known destination to increase GTO abilities for discovering various computational spaces. Here, the factor (Pr) needs to be provided in the range of [0:1] preceding the optimizing technique. If a factor (Pr) is superior to a random value, the movement to an uncertain position strategy is chosen. In addition, when a random integer is higher than or equivalent to fifty percent, a movement in the path of a recognizable position is selected, whereas a random integer is lesser than fifty percent, and a movement in a path of an identified site is decided. The three exploratory strategies are modelled mathematically in the following:

$$GX(g+1) = \begin{cases} LL + rd_1 \times (UL - LL), & Pr > rand, \\ H \times L + X_r(g) \times (rd_2 - C), & 0.5 \leq rand, \\ X(g) + \big(X(g) - GX_r(t)\big) \times rd_3 - (X(g) - GX_r(g) \times L^2), & 0.5 > rand \end{cases} \quad (2)$$

$$C = F \times \left(1 - \frac{Iter}{MaxIter}\right), \quad (3)$$

$$F = \cos(2 \times rd_4) + 1, \quad (4)$$

$$L = C \times l \quad (5)$$

$$H = Z \times X(g) \quad (6)$$

$$Z = [-C, C]. \quad (7)$$

3.3.2. Exploitation Phase

Two strategies are employed in the exploitation phase of GTO: competing for female adults and following the silverback. According to the C factor and conflicting them to the parameter (W) (that is altered), one of the two approaches is designated. The leader of the gorillas' group is the silverback that makes choices and directs others to food sources. When the C is higher than or equivalent to the W, this strategy is selected, and it is explained in the following.

$$GX(g+1) = L \times M(g) \times (X(g) - X_{siverback}) + X(g) \quad (8)$$

$$M(g) = \left(\left| \left(\frac{1}{N}\right) \sum_{i=1}^{N} G\, X_i(g) \right|^{2^L} \right)^{\left(\frac{1}{2L}\right)} \quad (9)$$

The second strategy is competing for female adults if C is lower than W, i.e., specialized for the assessment phase. As soon as adolescent gorillas reach adolescence, they engage in a violent rivalry with others for selecting females, and such behaviors are expressed in the following:

$$GX(g) = X_{silverback} - (X_{silverback} \times Q - X(g) \times Q) \times A\,(10)Q = 2 \times rd_5 - 1 \quad (11)$$

$$A = \beta \times E \quad (12)$$

$$E = \begin{cases} N_1 \; rand \geq 0.5 \\ N_2 \; rand < 0.5 \end{cases} \quad (13)$$

Eventually, at the exploitation phase, the cost of $GX(g)$ is compared to counterpart X (g). When the cost of $GX(g)$ is lower than X (g), then $GX(g)$ solution replaces them and becomes the optimum option (silverback).

The GTO system develops a fitness function (FF) for achieving maximal classifier performances. It defined a positive numeral for indicating the best efficiency of candidate results. In this case, the minimized classifier error rate was supposed to be provided by FF in Eq. (14). An optimum result is a lesser error rate, and the worst result gains a maximal error rate.

$$fitness(x_i) = ClassifierErrorRate(x_i) = \frac{number\ of\ misclassified\ samples}{Total\ number\ of\ samples} * 100 \quad (14)$$

3.4. Image Classification using SSAE Model

At last, the SSAE method can be implemented to categorize the class labels of the input HIs. The basic component for SSAE, AE, work for training feed-forward nonlinear neural network [20]. It comprises three important layers: output, hidden, and input. Multiple nodes frame all the AE layers; the node establishes a full connection among the nodes of the neighboring layer. The input layer representation is encoded in the encoder phase for connecting the input and AE hidden layers. On the other hand, the AE indicates the input layer reconstructed from encoding feature learning in the hidden layer in the decoder phase. The AE aims to determine the input dataset presentation utilized for creating the best reconstruction. A concatenated vector feature of the image patch was given to AE in this technique. Input image patches $\boldsymbol{x_i}$ was provided to AE in training, and reduced the error factor for each network connection weight was implemented by:

$$Arg\mathrm{Min}_{W,b,\widehat{W},\hat{b}} \sum_{i=1}^{N} | x_i - \left(\widehat{W}\left(\sigma(W x_i + b)\right) + \hat{b}\right) \quad (15)$$

Where band σ indicates the weight, bias, and activation function of the AE parameter. Assume an input layer x_i; the AE initially encodes the input to their presentation $h_i=\sigma(W_i+b)$, whereby $h_i$indicatesthe x_i response of hidden-layer neuron and h indicates the dimension that corresponds to the neuron count in the hidden state. The AE decodes the new input from the encoded learning all over the decoder phase, $\widehat{W}h_i + \hat{b}$. Instead of the constraint of hidden state dimension, an alternative method named sparse AE (SAE) imposed sparsity regularity on the AE hidden layer. SAE implements the regularity of the hidden layer response to prevent trivial solutions, which the fundamental AE tends toward. The fundamental AE requires the hidden layer dimension to be lesser when compared to the input layer dimension. Accurately, for making infinitesimal, the sparsity regularity is imposed on the AE. To construct a balance among the hidden state sparsity and reconstructed power for all the input nodes, the most appropriate hidden node response that drives the SAE for representing the trained set-in sparse feature is defined by:

$$ArgMin_{W,b,\widehat{W},\hat{b}} \sum_{i=1}^{N} \left| x_i - \left(\widehat{W}\left(\sigma(W x_i - b)\right) + \hat{b}\right) \right|_2^2 + \delta \sum_{j=1}^{M} K\, L(\rho | \rho^j) \quad (16)$$

$$KL(\rho | \rho^j) = \rho log \frac{\rho}{\rho^j} + (1-\rho) log^{\frac{1-\rho}{1-\rho^j}}, \quad (17)$$

From the equation, δ illustrates the balancing variable among sparsity and reconstruction, and the dimension of the hidden layers is determined as$M$. The$(\rho|\rho^j)$, called as Kullback-Leibler equation in (Eq. (17)), illustrates the divergence in two Bernoulli distributions that have the probabilities ρ andρ^j. Fig. 2 illustrates the infrastructure of SSAE.

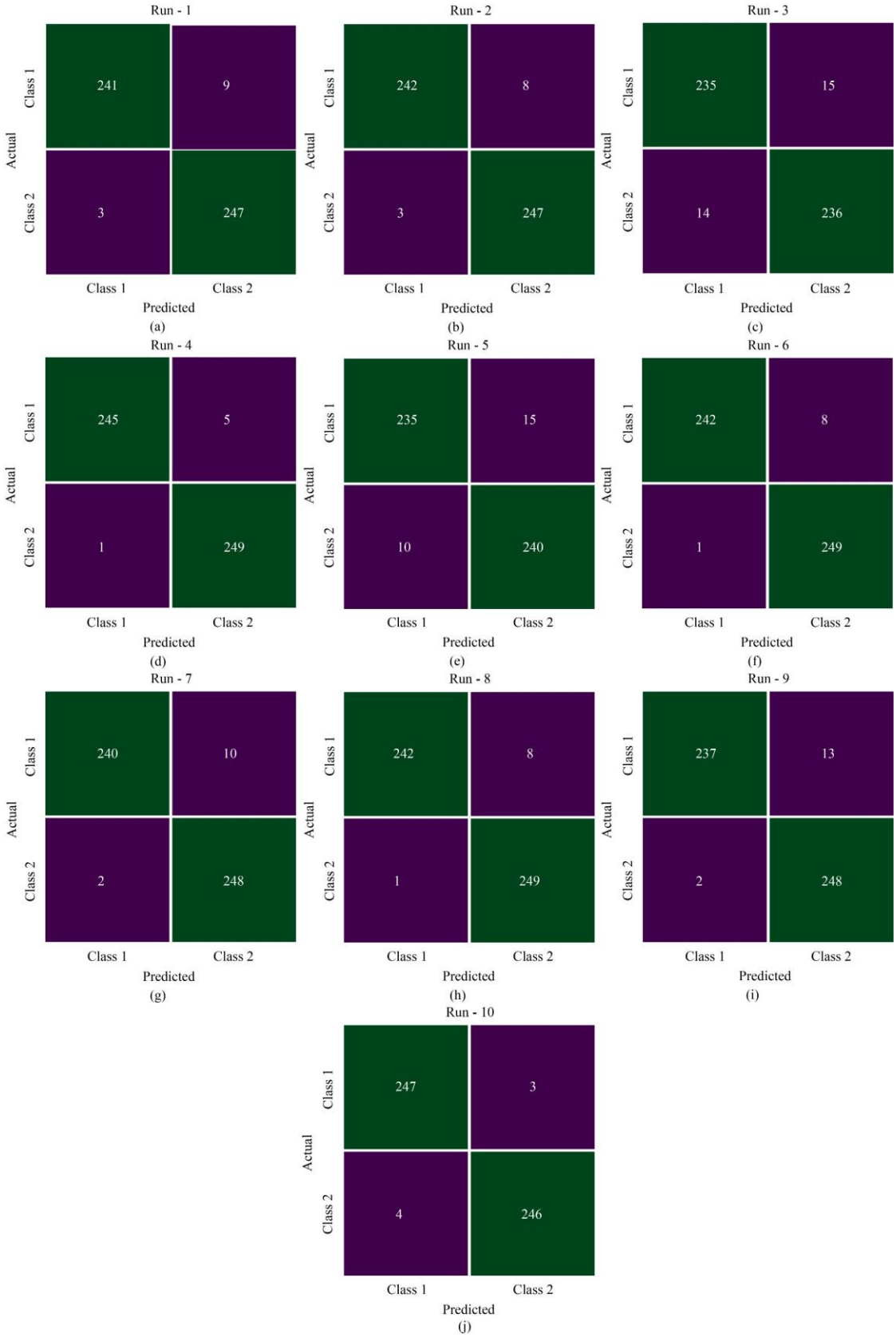

Fig. 3 Confusion matrices of GTODL-TCHI approach (a) Run-1, (b) Run-2, (c) Run-3, (d) Run-4, (e) Run-5, (f) Run-6, (g) Run-7, (h) Run-8, (i) Run-9, and (j) Run-10

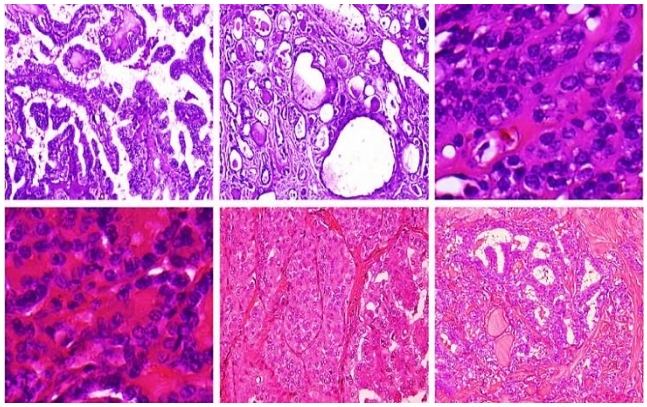

Fig. 4 Sample Histopathological Images

4. Result and Discussion

In this study, the performance validation of the GTODL-TCHI model is tested using a set of HIs. The dataset comprises 500 images under two class labels, as depicted in Table 1. Fig. 4 demonstrates the sample Histopathological images.

Table 1. Dataset details

Class Label	Class Name	No. of Images
Class 1	Normal Thyroid (NT)	250
Class 2	Papillary Thyroid Carcinoma (PTC)	250
Total No. of Images		**500**

Fig. 3 reports a set of confusion matrices produced by the GTODL-TCHI model on ten runs of execution. On run-1, the GTODL-TCHI model has recognized 241 samples in class 1 and 247 samples in class 2. Also, on run-3, the GTODL-TCHI technique has recognized 235 samples into class 1 and 236 samples into class 2. In addition, on run-5, the GTODL-TCHI method has recognized 235 samples into class 1 and 240 samples into class 2. Moreover, on run-6, the GTODL-TCHI approach recognized 242 samples in class 1 and 249 samples in class 2. Furthermore, on run-9, the GTODL-TCHI methodology recognized 237 samples in class 1 and 248 samples in class 2. At last, on run-10, the GTODL-TCHI algorithm recognized 247 samples in class 1 and 246 samples in class 2.

Table 2 offers extensive thyroid classification outcomes of the GTODL-TCHI model under ten distinct runs. Fig. 5 illustrates the overall classifier results of the GTODL-TCHI model underruns 1-5. The figure pointed out that the GTODL-TCHI model has resulted in enhanced results under all classes. For instance, on run-1, the GTODL-TCHI model has provided average $accu_y$ of 97.60%, $sens_y$ of 97.60%, $spec_y$ of 97.60%, F_{score} of 97.60%, and MCC of 95.23%. Meanwhile, on run-1, the GTODL-TCHI method has offered average $accu_y$ of 98.60%, $sens_y$ of 98.60%, $spec_y$ of 98.60%, F_{score} of 98.60%, and MCC of 97.20%. Eventually, on run-4, the GTODL-TCHI approach provided average $accu_y$ of 94.20%, $sens_y$ of 94.20%, $spec_y$ of 94.20%, F_{score} of 94.20%, and MCC of 88.40%. At last, on run-5, the GTODL-TCHI technique has rendered average $accu_y$ of 98.80%, $sens_y$ of 98.80%, $spec_y$ of 98.80%, F_{score} of 98.80%, and MCC of 97.61%.

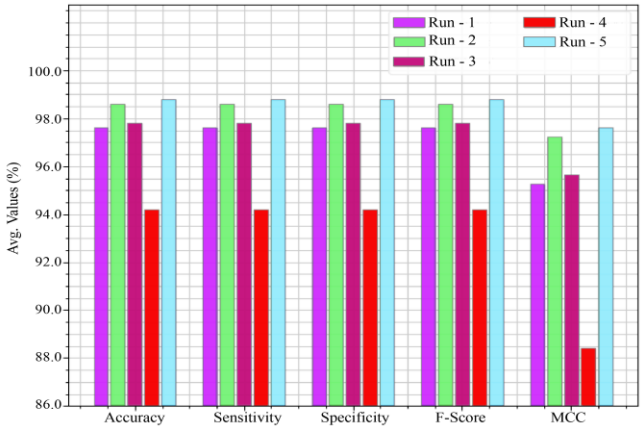

Fig. 5 Average analysis of GTODL-TCHI approach underruns 1-5

Fig. 6 demonstrates the overall classifier results of the GTODL-TCHI method underruns 6-10. The figure denoted that the GTODL-TCHI technique has resulted in enhanced results under all classes. For example, on run-6, the GTODL-TCHI approach has rendered average $accu_y$ of 95%, $sens_y$ of 95%, $spec_y$ of 95%, F_{score} of 95%, and MCC of 90.02%. At the same time, on run-8, the GTODL-TCHI methodology has provided average $accu_y$ of 97.60%, $sens_y$ of 97.60%, $spec_y$ of 97.60%, F_{score} of 97.60%, and MCC of 95.25%. Finally, on run-9, the GTODL-TCHI algorithm has granted average $accu_y$ of 98.20%, $sens_y$ of 98.20%, $spec_y$ of 98.20%, F_{score} of 98.20%, and MCC of 96.44%. At last, on run-10, the GTODL-TCHI method has presented average $accu_y$ of 97%, $sens_y$ of 97%, $spec_y$ of 97%, F_{score} of 97%, and MCC of 94.09%.

Table 2. Result analysis of GTODL-TCHI approach with various measures and runs

Class Labels	Accuracy	Sensitivity	Specificity	F-Score	MCC
Run - 1					
Class 1	97.60	96.40	98.80	97.57	95.23
Class 2	97.60	98.80	96.40	97.63	95.23
Average	**97.60**	**97.60**	**97.60**	**97.60**	**95.23**
Run - 2					
Class 1	98.60	98.80	98.40	98.60	97.20
Class 2	98.60	98.40	98.80	98.60	97.20
Average	**98.60**	**98.60**	**98.60**	**98.60**	**97.20**
Run - 3					
Class 1	97.80	96.80	98.80	97.78	95.62
Class 2	97.80	98.80	96.80	97.82	95.62
Average	**97.80**	**97.80**	**97.80**	**97.80**	**95.62**
Run - 4					
Class 1	94.20	94.00	94.40	94.19	88.40
Class 2	94.20	94.40	94.00	94.21	88.40
Average	**94.20**	**94.20**	**94.20**	**94.20**	**88.40**
Run - 5					
Class 1	98.80	98.00	99.60	98.79	97.61
Class 2	98.80	99.60	98.00	98.81	97.61
Average	**98.80**	**98.80**	**98.80**	**98.80**	**97.61**
Run - 6					
Class 1	95.00	94.00	96.00	94.95	90.02
Class 2	95.00	96.00	94.00	95.05	90.02
Average	**95.00**	**95.00**	**95.00**	**95.00**	**90.02**
Run - 7					
Class 1	98.20	96.80	99.60	98.17	96.44
Class 2	98.20	99.60	96.80	98.22	96.44
Average	**98.20**	**98.20**	**98.20**	**98.20**	**96.44**
Run - 8					
Class 1	97.60	96.00	99.20	97.56	95.25
Class 2	97.60	99.20	96.00	97.64	95.25
Average	**97.60**	**97.60**	**97.60**	**97.60**	**95.25**
Run - 9					
Class 1	98.20	96.80	99.60	98.17	96.44
Class 2	98.20	99.60	96.80	98.22	96.44
Average	**98.20**	**98.20**	**98.20**	**98.20**	**96.44**
Run - 10					
Class 1	97.00	94.80	99.20	96.93	94.09
Class 2	97.00	99.20	94.80	97.06	94.09
Average	**97.00**	**97.00**	**97.00**	**97.00**	**94.09**

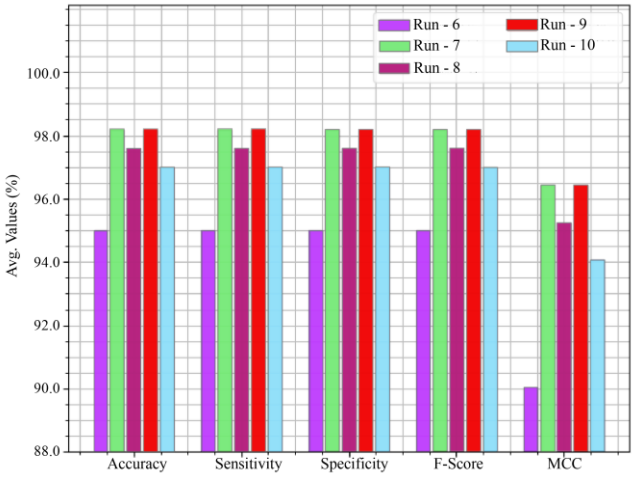

Fig. 6 Average analysis of GTODL-TCHI approach underruns 6-10

The training accuracy (TA) and validation accuracy (VA) acquired by the GTODL-TCHI methodology on the test dataset is illustrated in Fig. 7. The experimental outcome denoted by the GTODL-TCHI methodology has gained maximal values of TA and VA. To be specific, the VA seemed to be higher than TA.

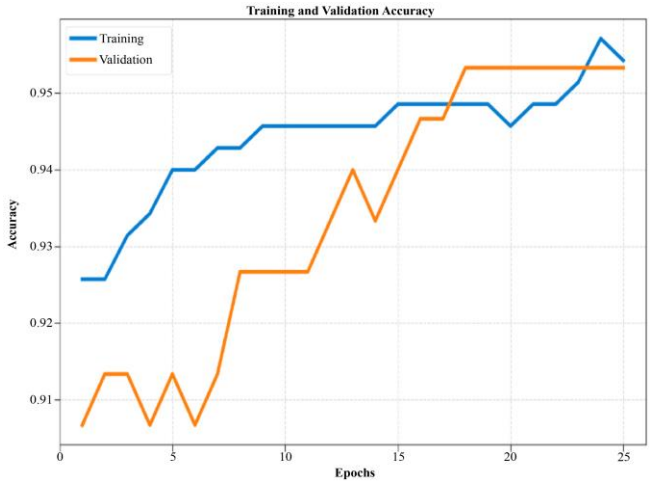

Fig. 7 TA and VA analysis of the GTODL-TCHI approach

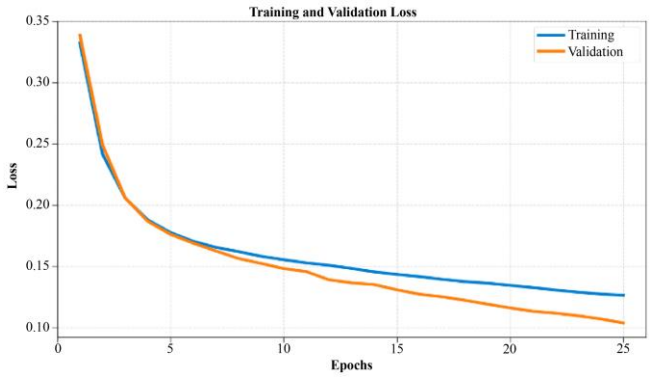

Fig. 8 TL and VL analysis of GTODL-TCHI approach

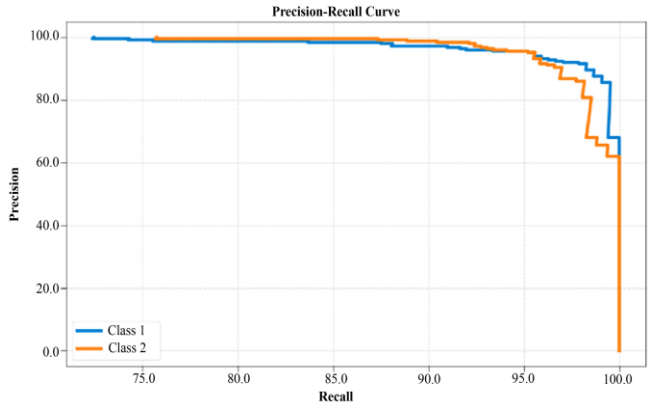

Fig. 9 Precision-recall curve analysis of the GTODL-TCHI approach

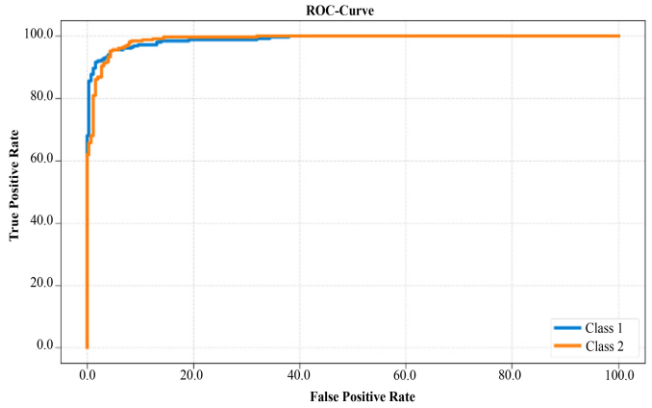

Fig. 10 ROC curve analysis of GTODL-TCHI approach

The training loss (TL) and validation loss (VL) attained by the GTODL-TCHI technique on the test dataset are established in Fig. 8. The experimental outcome inferred that the GTODL-TCHI approach had accomplished the least values of TL and VL. Particularly, the VL is lower than TL.

A clear precision-recall examination of the GTODL-TCHI technique on the test dataset is depicted in Fig. 9. The figure specified that the GTODL-TCHI approach has resulted in enhanced values of precision-recall values under all classes.

A brief ROC analysis of the GTODL-TCHI algorithm on the test dataset is portrayed in Fig. 10. The results represented that the GTODL-TCHI approach has shown its ability to categorize distinct classes on the test dataset.

Table 3. Comparative analysis of GTODL-TCHI approach with recent algorithms

Methods	Sensitivity	Specificity	Accuracy
GTODL-TCHI	98.80	98.80	98.80
NB-CMR	94.08	96.62	94.86
SVMQ-NB	91.62	98.20	94.28
SVML-CMR	98.19	97.59	97.89
SVML-SVMQ	97.49	98.54	97.99
SVMRBF-NBCMR	97.69	97.47	93.60

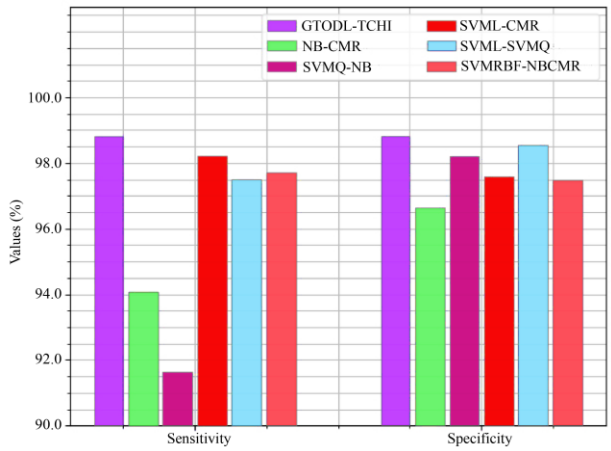

Fig. 11 $Sens_y$ And $spec_y$ analysis of the GTODL-TCHI approach with recent algorithms

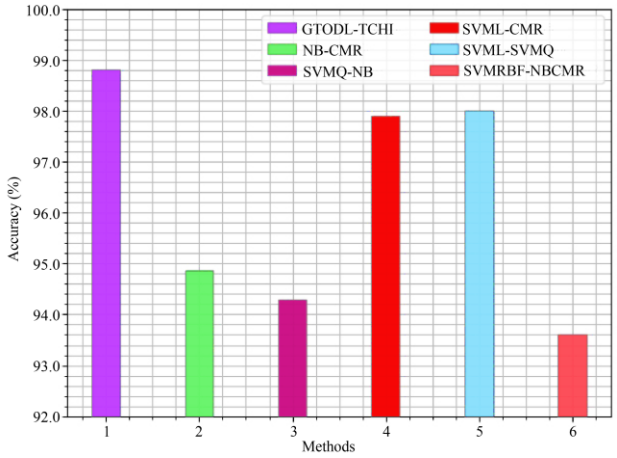

Fig. 12 $Accu_y$ Analysis of GTODL-TCHI approach with recent algorithms

Table 3 portrays an overall comparative thyroid classification performance of the GTODL-TCHI model with existing models [21]. Fig. 11 shows the comparison study of the GTODL-TCHI method with recent models in terms of $sens_y$and $spec_y$. The results represented the SVMRBF-NBCMR approach has shown poor performance with minimum $sens_y$ and $spec_y$ value. Meanwhile, the NB-CMR and SVMQ-NB methodologies have gained slightly enhanced values of $sens_y$and$spec_y$. Next, the SVML-CMR and SVML-SVMQ algorithms have resulted in reasonable $sens_y$ and $spec_y$ values. But, the GTODL-TCHI model has shown an effectual outcome with maximum $sens_y$ and $spec_y$ of 98.80% and 98.80% correspondingly.

Fig. 12 depicts the comparison study of the GTODL-TCHI model with recent models in terms of$accu_y$. The results inferred that the SVMRBF-NBCMR model had shown poor performance with minimum $accu_y$ value. At the same time, the NB-CMR and SVMQ-NB models have obtained slightly enhanced values of$accu_y$. Followed by the SVML-CMR and SVML-SVMQ models have resulted in reasonable $accu_y$ values. However, the GTODL-TCHI model has shown an effectual outcome with maximum $accu_y$ of 98.80%.

Therefore, the experimental results and discussion portrayed that the GTODL-TCHI model has revealed effectual thyroid classification performance over other models.

5. Conclusion

In this study, a new GTODL-TCHI model was advanced to recognize the presence of the thyroid on HIs. The presented GTODL-TCHI model primarily utilized the NLMF technique to eradicate the existence of noise, and then the FCN model was utilized to segment the images.

Then, the DenseNet-121 technique is utilized for deriving feature vectors, and the use of the GTO algorithm tunes its hyperparameters. At last, the SSAE model is applied to categorize the class labels of the input HIs. The performance validation of the GTODL-TCHI method is tested using a HI dataset, and the results reported a significant performance over the recent state of art DL models.

Therefore, the GTODL-TCHI model can be treated as an effectual CAD model for thyroid classification. Hybrid DL classifiers will be applied in the upcoming years to boost classification performance.

References

[1] Vijaya Gajanan Buddhavarapu, and Angel Arul Jothi J, "An Experimental Study on Classification of Thyroid Histopathology Images Using Transfer Learning," *Pattern Recognition Letters*, vol. 140, pp. 1-9, 2020. *Crossref*, https://doi.org/10.1016/j.patrec.2020.09.020

[2] Bing Han et al., "Automatic Classification Method of Thyroid Pathological Images Using Multiple Magnification Factors," *Neurocomputing*, vol. 460, pp. 231-242, 2021. *Crossref*, https://doi.org/10.1016/j.neucom.2021.07.024

[3] Pingjun Chen et al., "Interactive Thyroid Whole Slide Image Diagnostic System Using Deep Representation," *Computer Methods and Programs in Biomedicine*, vol. 195, p. 105630. *Crossref*, https://doi.org/10.1016/j.cmpb.2020.105630

[4] Junho Song, "Ultrasound Image Analysis Using Deep Learning Algorithm for the Diagnosis of Thyroid Nodules," *Medicine*, vol. 98, no. 15, p. e15133, 2019. *Crossref*, https://doi.org/10.1097%2FMD.0000000000015133

[5] Akila Victor et al., "Detection and Classification of Breast Cancer Using Machine Learning Techniques for Ultrasound Images," *International Journal of Engineering Trends and Technology*, vol. 70, no. 3, pp. 170-178, 2022. *Crossref*, https://doi.org/10.14445/22315381/IJETT-V70I3P219

[6] Xiangchun Li et al., "Diagnosis of Thyroid Cancer Using Deep Convolutional Neural Network Models Applied to Sonographic Images: A Retrospective, Multicohort, Diagnostic Study," *The Lancet Oncology*, vol. 20, no. 2, pp. 193-201, 2019. *Crossref*, https://doi.org/10.1016/S1470-2045(18)30762-9

[7] Martin Halicek, "Tumor Detection of the Thyroid and Salivary Glands Using Hyperspectral Imaging and Deep Learning," *Biomedical Optics Express*, vol. 11, no. 3, pp. 1383-1400, 2020. *Crossref*, https://doi.org/10.1364/BOE.381257

[8] Ahmed Sharafeldeen, "Texture and Shape Analysis of Diffusion-Weighted Imaging for Thyroid Nodules Classification Using Machine Learning," *Medical Physics*, vol. 49, no. 2, pp. 988-999, 2022.*Crossref*, https://doi.org/10.1002/mp.15399

[9] Bijaya Kumar Hatuwal, and Himal Chand Thapa, "Lung Cancer Detection Using Convolutional Neural Network on Histopathological Images," *International Journal of Computer Trends and Technology*, vol. 68, no. 10, pp. 21-24, 2020. *Crossref*, https://doi.org/10.14445/22312803/IJCTT-V68I10P104

[10] Nguyen Thanh Duc et al., "An Ensemble Deep Learning for Automatic Prediction of Papillary Thyroid Carcinoma Using Fine Needle Aspiration Cytology," Expert Systems with Applications, vol. 188, p. 115927, 2022. *Crossref*, https://doi.org/10.1016/j.eswa.2021.115927

[11] Bing Han et al., "Automatic Classification Method of Thyroid Pathological Images Using Multiple Magnification Factors," *Neurocomputing*, vol. 460, pp. 231-242, 2021. *Crossref*, https://doi.org/10.1016/j.neucom.2021.07.024

[12] Zihan Wu, "Direct Prediction of BRAFV600E Mutation from Histopathological Images in Papillary Thyroid Carcinoma with a Deep Learning Workflow," *2020 4th International Conference on Computer Science and Artificial Intelligence*, pp. 146-151, 2020. *Crossref*, https://doi.org/10.1145/3445815.3445840

[13] Yonghua Wang, Wei Ke, and Pin Wan "A Method of Ultrasonic Image Recognition for Thyroid Papillary Carcinoma Based on Deep Convolution Neural Network," *Neuroquantology*, vol. 16, no. 5, 2018. *Crossref*, http://dx.doi.org/10.14704/nq.2018.16.5.1306

[14] Tianjiao Liu et al., "Classification of Thyroid Nodules in Ultrasound Images Using Deep Model Based Transfer Learning and Hybrid Features," *2017 IEEE International Conference on Acoustics, Speech and Signal Processing (ICASSP)*, pp. 919-923, 2017. *Crossref*, https://doi.org/10.1109/ICASSP.2017.7952290

[15] Jianning Chi et al., "Thyroid Nodule Classification in Ultrasound Images by Fine-Tuning Deep Convolutional Neural Network," *Journal of Digital Imaging*, vol. 30, no. 4, pp. 477-486, 2017. *Crossref*, https://doi.org/10.1007/s10278-017-9997-

[16] Anish Anurag et al., "Local Attention-Based Descriptor Definition Using Vision Transformer for Breast Cancer Identification," *International Journal of Engineering Trends and Technology*, vol. 70, no. 12, pp. 317-327, 2022. *Crossref*, https://doi.org/10.14445/22315381/IJETT-V70I12P230

[17] Babak Kashir, "Application of Fully Convolutional Neural Networks for Feature Extraction in Fluid Flow," *Journal of Visualization*, vol. 24, no. 4, pp.771-785, 2021. *Crossref*, https://doi.org/10.1007/s12650-020-00732-0

[18] Tavishee Chauhan, Hemant Palivela, and Sarveshmani Tiwari, "Optimization and Fine-Tuning of Densenet Model for Classification of Covid-19 Cases in Medical Imaging," *International Journal of Information Management Data Insights*, vol. 1, no. 2, p.100020, 2021. *Crossref*, https://doi.org/10.1016/j.jjimei.2021.100020

[19] J. Antogerminsweeta, and Dr. B. Sivagami, "Contemporary Techniques in Digital Image Processing," *SSRG International Journal of Computer Science and Engineering* , vol. 6, no. 11, pp. 43-46, 2019. *Crossref*, https://doi.org/10.14445/23488387/IJCSE-V6I11P109

[20] Zhezhe Han et al., "Combustion Stability Monitoring Through Flame Imaging and Stacked Sparse Autoencoder Based Deep Neural Network," *Applied Energy*, vol. 259, p.114159

[21] Angel Arul Jothi J, and Mary Anita Rajam V, "Automatic Classification of Thyroid Histopathology Images Using Multi-Classifier System," *Multimedia Tools and Applications*, vol. 76, no. 18, pp.18711-18730, 2017. *Crossref*, https://doi.org/10.1007/s11042-017-4363-0

[22] Kirubha. M et al., "Analysis of Thyroid Disease Using K Means and Fuzzy C Means Algorithm," *SSRG International Journal of Computer Science and Engineering*, vol. 6, no. 10, pp. 1-6, 2019. *Crossref*, https://doi.org/10.14445/23488387/IJCSE-V6I10P101

[23] Mei Yu et al., "Adaptive Soft Erasure with Edge Self-Attention for Weakly Supervised Semantic Segmentation: Thyroid Ultrasound Image Case Study," *Computers in Biology and Medicine*, vol. 144, p. 105347, 2022. *Crossref*, https://doi.org/10.1016/j.compbiomed.2022.105347

[24] Peiling Tsou, and Chang-Jiun Wu, "Mapping Driver Mutations to Histopathological Subtypes in Papillary Thyroid Carcinoma: Applying a Deep Convolutional Neural Network," *Journal of Clinical Medicine*, vol. 8, no. 10, p.1675, 2019. *Crossref*, https://doi.org/10.3390%2Fjcm8101675

[25] M. C. Shanker, and M. Vadivel, "Hybrid Transfer Learning of Mammogram Images for Screening of Micro-Calcifications," *SSRG International Journal of Electrical and Electronics Engineering*, vol. 9, no. 8, pp. 40-47, 2022. *Crossref*, https://doi.org/10.14445/23488379/IJEEE-V9I8P105

[26] Haitao Song et al., "Rapid Identification of Papillary Thyroid Carcinoma and Papillary Microcarcinoma Based on Serum Raman Spectroscopy Combined with Machine Learning Models," *Photodiagnosis and Photodynamic Therapy*, vol. 37, p.102647, 2022. *Crossref*, https://doi.org/10.1016/j.pdpdt.2021.102647

[27] Ahmed Ginidi et al., "Gorilla Troops Optimizer for Electrically Based Single and Double-Diode Models of Solar Photovoltaic Systems," *Sustainability*, vol. 13, no. 16, p. 9459, 2021.